Appl. Phys. A (2017) 123:573
DOI 10.1007/s00339-017-1180-2

Applied Physics A
Materials Science & Processing

CrossMark

Performance of Erbium-doped TiO_2 thin film grown by physical vapor deposition technique

Rini Lahiri[1] · Anupam Ghosh[2] · Shyam Murli Manohar Dhar Dwivedi[2] · Shubhro Chakrabartty[2] · P. Chinnamuthu[1] · Aniruddha Mondal[2]

Received: 12 May 2017 / Accepted: 29 July 2017 / Published online: 8 August 2017
© Springer-Verlag GmbH Germany 2017

Abstract Undoped and Erbium-doped TiO_2 thin films ($Er:TiO_2$ TFs) were fabricated on the n-type Si substrate using physical vapour deposition technique. Field emission scanning electron microscope showed the morphological change in the structure of $Er:TiO_2$ TF as compared to undoped sample. Energy dispersive X-ray spectroscopy (EDX) confirmed the Er doping in the TiO_2 thin film (TF). The XRD and Raman spectrum showed the presence of anatase phase TiO_2 and Er_2O_3 in the $Er:TiO_2$ TF. The Raman scattering depicted additional number of vibrational modes for $Er:TiO_2$ TF due to the presence of Er as compared to the undoped TiO_2 TF. The UV–Vis absorption measurement showed that $Er:TiO_2$ TF had approximately 1.2 times more absorption over the undoped TiO_2 TF in the range of 300–400 nm. The main band transition, i.e., the transition between the oxygen (2p) state and the Ti (3d) state was obtained at $\sim$3.0 eV for undoped TiO_2 and at $\sim$3.2 eV for $Er:TiO_2$ TF, respectively. The photo responsivity measurement was done on both the detectors, where $Er:TiO_2$ TF detector showed better detectivity (D^*), noise equivalent power and temporal response as compared to undoped detector under ultra-violet illumination.

✉ Aniruddha Mondal
aniruddhamo@gmail.com

[1] Department of Electronics and Communication Engineering, National Institute of Technology Nagaland, Dimapur 797103, India

[2] Department of Physics, National Institute of Technology Durgapur, Durgapur 713209, India

1 Introduction

In recent years, UV photodetectors have been studied for a wide range of applications in the field related to military applications such as flame detection [1] and other applications like optical communication [2] and astronomical studies [3]. Previously, silicon photodiodes were used for UV photodetection but it failed to detect UV light with high sensitivity [4]. To overcome these limitations, wide band gap materials was studied such as SiC [5, 6], III-nitrides like GaN [7, 8], AlGaN [9] and most of the II–VI compounds like ZnO [10, 11] and metal oxides like TiO_2 and In_2O_3 [12, 13]. But the UV detectors fabricated by the oxide materials are detecting both UV light as well as visible light due to the presence of oxygen-related defects [14]. Therefore, the responsivity in the UV region has been decreased for such materials. TiO_2 is a wide band gap semiconductor available in the form of Rutile (3 eV), Brookite (3.13 eV) and Anatase (3.21 eV) as reported by Coronado et al. [15]. It is used for various applications in solar cell [16], biosensors [17], photocatalysis [18], cancer therapy [19, 20] and UV detectors [21, 22]. For anatase TiO_2, the conduction band is mainly made from the unoccupied Ti 3d states. Morgan and Watson [23] reported that the O vacancy produced a single gap-state peak 1.5 eV below the conduction band minimum for an anatase TiO_2 which was due to the excess electrons occupied by the two Ti 3d orbitals, where one of these occupied Ti sites was near the vacancy and the second was present at the next nearest Ti position. Split vacancy geometry was obtained when oxygen from the nearest Ti sites moved towards this vacancy. The authors further showed that the oxygen defect reduces the optical band gap due to the d–d splitting between the unoccupied and occupied Ti 3d states making it susceptible to the visible light detection. To remove the

oxygen defects and improve detectivity in the UV region, TiO_2 has been doped with suitable elements. Rare earth elements are studied extensively due to its optical properties. Er is one such rare earth element which has been studied mainly for its upconversion properties [24, 25] and in various applications such as Er-doped fiber amplifier (EDFA) [26], lasers [27] and LEDs [28]. Recently, it has been reported that the Er doping in In_2O_3 enhances the band gap, UV sensitivity and removes the oxygen defect simultaneously [29]. But there is no single report on the Er:TiO_2 for the enhancement of UV detection sensitivity.

In this paper, we have reported the fabrication of undoped and Er:TiO_2 TFs on Si substrate by electron beam evaporator technique. The structural morphology of both the TFs was studied using field emission scanning electron microscope (FESEM) and energy dispersive X-ray spectroscopy (EDX) confirmed the doping of Er into the TiO_2 lattice. The optical measurements showed the improvement in UV light absorption for Er:TiO_2 as compared to the undoped TiO_2 TF. Further, electrical measurements were done on Si/TiO_2 TF/Au and Si/Er:TiO_2 TF/Au detectors and showed improved detector characteristics and parameters for the latter case under UV illumination.

2 Experimental details

2.1 Synthesis of TiO_2 and Er:TiO_2 TFs and optical detector

The TiO_2 and Er:TiO_2 TFs were deposited using e-beam evaporation system (BC-300, HHV, India). The Er:TiO_2 pellets were prepared by mixing one-third of Er_2O_3 (99.995% purity, Equipment support company, USA) with two-third of TiO_2 (99.995% purity, Equipment support company, USA) with polyvinyl alcohol and hydraulic pressed for 15 min. The silicon substrates were cleaned by RCA method. The e-beam evaporation technique was used to deposit 50-nm thick TiO_2 and Er:TiO_2 TFs on two separate n-type silicon substrate at a constant rate of evaporation of material ~ 0.12 nm s^{-1} and the base pressure of nearly 6.5×10^{-6} mbar. The rate of deposition and the thickness are monitored by the digital thickness monitor (DTM) crystal present in the e-beam chamber. The as-deposited samples were then annealed in muffle furnace (KL-1500X, MTI Corporation) at 500 °C for 1 h. To fabricate the detectors, Au contacts were deposited on the top of undoped TiO_2 and Er:TiO_2 TFs. The Au material on the TFs was deposited through aluminum mask hole of diameter around 1 mm.

The FESEM (Carl Zeiss, sigma), EDX (ZEISS EVO-MA10) and X-Ray diffraction (Rigaku Ultima IV; using Cu Kα radiation) were done on the samples. The optical absorption measurement was performed on the samples by a UV–Visible-Near-infrared spectrophotometer (Lambda 950, Perkin Elmer) using specular reflection method. The vibrational modes of the system were investigated using triple Raman Spectrometer (T64000, J-Y Horiba) using Ar^+ laser of 532 nm excitation wavelength. The current (I)–voltage (V) characteristics and photocurrent spectrum of the TiO_2 TF-based detector were investigated using a Keithley 2401 source-measure unit and 300 W Xenon arc lamp (650-0047) through a monochromator (Sciencetech Inc., Canada).

3 Results and discussion

3.1 Structural and Raman analysis

3.1.1 FESEM, EDX and XRD analysis

Figure 1a, b shows the top view of FESEM image of undoped and Er:TiO_2 film, respectively. It is observed that the grain boundaries are well defined in case of undoped TiO_2 TF but are broken when the TiO_2 is doped with Er. This shows that the Er doping affected the morphology of the pure TiO_2 material. The similar effects also have been observed for the case of In-doped TiO_2 TF prepared by e-beam evaporation technique [30].

Figure 1c shows the EDX spectrum of the undoped and Er:TiO_2. The undoped sample shows the presence of titanium (Ti), oxygen (O_2) silicon (Si), whereas Er:TiO_2 sample, shows the presence of Er along with Ti, O_2 and Si. The fact confirms the doping of TiO_2 with Er. Figure 2 shows the XRD pattern of the both undoped and Er:TiO_2 thin film. In undoped sample the diffraction from Anatase phase (101), (221), (105), (211), (215) [JCPDS 89-4921] and (114), (204) [JCPDS 89-4203] of TiO_2 and in Er:TiO_2 sample peaks for Er_2O_3 (024) [JCPDS 77-0777] and (156) [JCPDS 77-0462] along with the TiO_2 peak is also observed. Similar presence of Er_2O_3 in XRD was also observed by Bender et al. [31] for Er:TiO_2 nanostructures. They reported the presence of $Er_2Ti_2O_7$ (ETO) too which was prominent only for high amount of doping which was not observed in our work due to less doping concentration of Er. The grain size for both the undoped TiO_2 and Er:TiO_2 films were calculated from XRD peaks using Scherrer formula [32] given by Eq. (1):

$$D = \frac{K\lambda}{\beta \cos\theta} \quad (1)$$

where D is the grain size, K is the Scherrer constant (0.9), λ is the wavelength of the X-ray (1.54 Å) and β is the full width half maximum (FWHM) of the spectrum taken in radians.

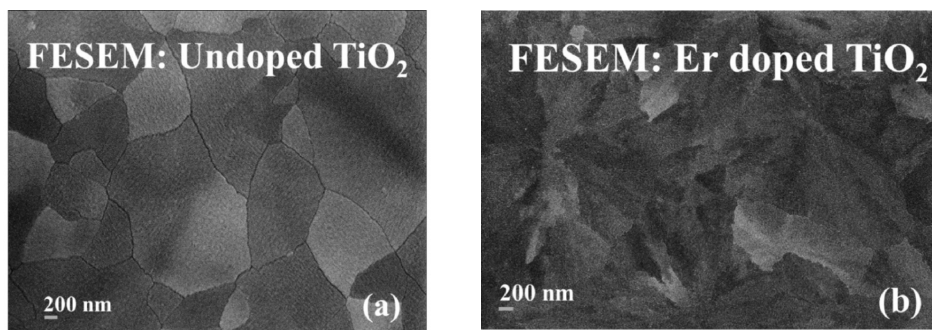

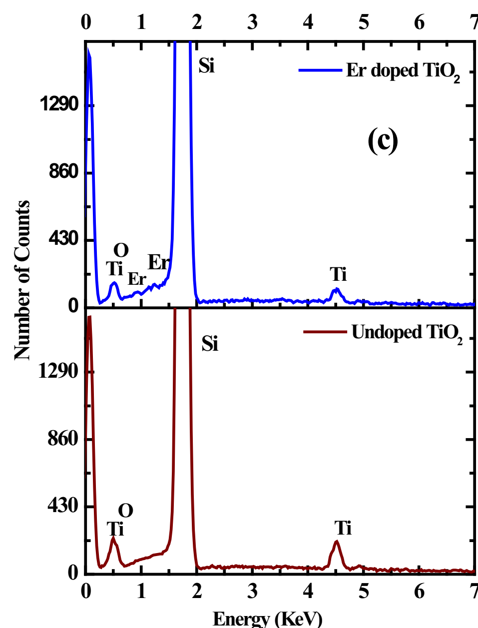

Fig. 1 Top view FESEM images of **a** undoped TiO_2 TF, **b** Er:TiO_2 TF and **c** EDX analysis

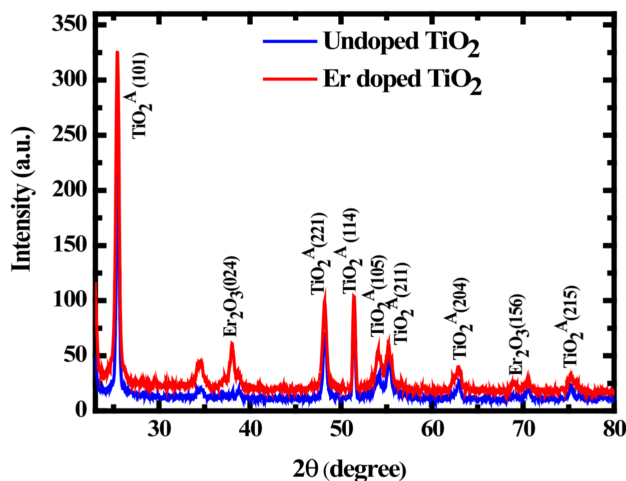

Fig. 2 XRD patterns of undoped and Er:TiO_2 TFs on Silicon substrate

The average grain size was observed to be around 22 nm for undoped TiO_2 which reduced to 18 nm for Er:TiO_2. For (101) anatase plane it decreased from 18 nm for undoped TiO_2 to 15 nm for Er:TiO_2. This reduced grain size was attributed to the disorder caused as a result of the substitution of Er^{3+} ions (0.0881 nm) in the Ti^{4+} (0.0605 nm) [33]. This verifies the doping of the TiO_2 film with Er.

3.1.2 Raman analysis

Figure 3 shows the Raman spectrum of the Er doped and undoped TiO_2 samples. The Raman spectrum of undoped sample shows the peaks at 143, 300, 512 and 635 cm^{-1}. The high intense peak at the 143 cm^{-1} and the low intense peak at the 635 cm^{-1} are recognized to be close to the E_g modes of 144 and 639 cm^{-1} of anatase TiO_2 [34] and this verifies the XRD results which shows that only the anatase phase of the TiO_2 is present. The Si peaks at 300 and 521 cm^{-1} are due to the silicon substrate. On the other hand, the Raman spectrum of Er:TiO_2 shows peaks around at 145, 170, 204, 211, 268, 300, 334, 343, 376, 402, 521, 597, 638, 695 and 745 cm^{-1}. The peaks at 300 and 521 cm^{-1} are also due to silicon substrate. The peaks at 145 and 638 cm^{-1} also corresponds to E_g mode of TiO_2

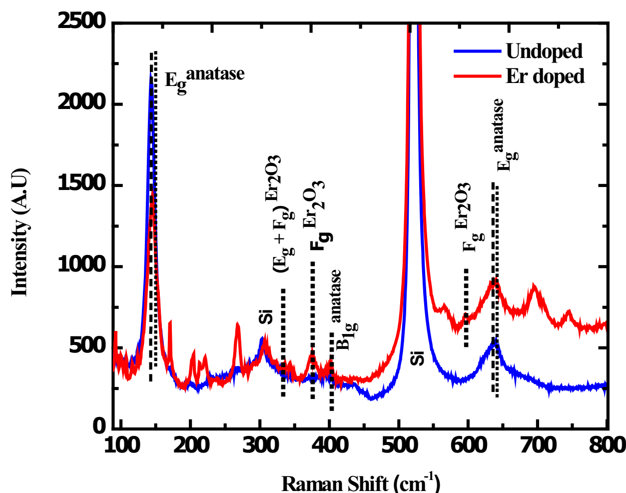

Fig. 3 Raman spectrum of undoped TiO_2 and Er:TiO_2 TFs

(close to 144 and 639 cm^{-1}) but shows a blue shift as compared to the undoped TiO_2 sample as reported elsewhere [35]. The peaks at 334, 376 and 597 cm^{-1} may correspond to the $E_g + F_g$ modes (334 cm^{-1}), F_g mode (379 cm^{-1}) and F_g mode (595 cm^{-1}) of Er_2O_3, respectively [36]. Palomino-Merino et al. [37] have reported that Er doping of TiO_2 imposed some new Raman bands which they assumed to be due to some minor structural deformation of the TiO_2 due to the incorporation of Er, which may be the same reason that new Raman bands were observed in our work.

3.2 Optical analysis

Optical absorption measurement was done at room temperature for the Er doped and undoped samples (Fig. 4a). The Er:TiO_2 shows large absorption in UV region (300–400 nm), which is enhanced by 1.2 times as compared to the undoped sample.

The Tauc plot $(\alpha h\nu)^2$ vs hν for both the undoped and Er doped sample is shown in Fig. 4b. The extrapolation from the linear part of the curves to the hν-axis shows the optical band gap of ~3.0 eV for undoped TiO_2 and ~3.2 eV for Er:TiO_2, respectively. The band gap of 3.0 eV for undoped TiO_2 indicates the main band transition between O (2p) valence band to Ti (3d) conduction band [38], which is near to the anatase TiO_2 band gap (3.21 eV). However, a decrease in the band gap may be due to annealing as reported by some other groups [39]. On the other hand, the Er:TiO_2 shows the blue shift of 0.2 eV in the band gap energy with respect to the undoped TiO_2 TF which is similar as authors have reported for the Er doped In_2O_3 TF prepared in sol–gel technique [29]. The band gap enhancement of TiO_2 due to Er doping may be due to the increase in the conduction band energy level and decrease in the valence band resulted from substitutional doping of Er in place of Ti into TiO_2 lattice. The transition at around 2 eV for undoped TiO_2 and 1.8 eV for Er:TiO_2 may be due to the sub-band gap related transitions, which related to Ti^{3+} defects [40]. In case of sol–gel grown Er doped In_2O_3 the Ti^{3+} defect has been removed with enhanced Er content into the lattice of In_2O_3 [29]. But in case of physical vapor deposition (PVD) technique such removal of defects has not been observed after Er doping. Therefore, it may be concluded that the removal of defects from oxide semiconductor materials by Er is basically process dependent. On the other hand the enhancement in UV light absorption has been improved by the Er:In_2O_3 TF as compared to In_2O_3 TF detector.

3.3 TiO_2 TF and Er:TiO_2 TF as UV detector

The Au/TiO_2 TF/n-Si and Au/Er:TiO_2 TF/n-Si detectors were characterized. Figure 5 shows the room temperature current (*I*) vs voltage (*V*) characteristics for both the detectors. The dark currents and photocurrents (under white light excitation, 300 W Xenon arc lamp) of the detectors were measured. The forward current density for the Er:TiO_2 is high (5.2×10^{-4} A cm^{-2} at +1.5 V) as

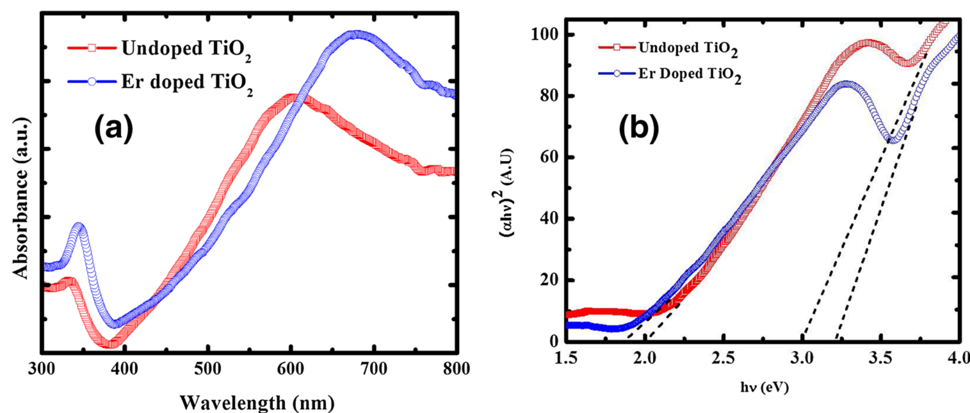

Fig. 4 **a** Optical absorption, **b** $(\alpha h\nu)^2$ vs hν plot of undoped TiO_2 and Er:TiO_2 TFs

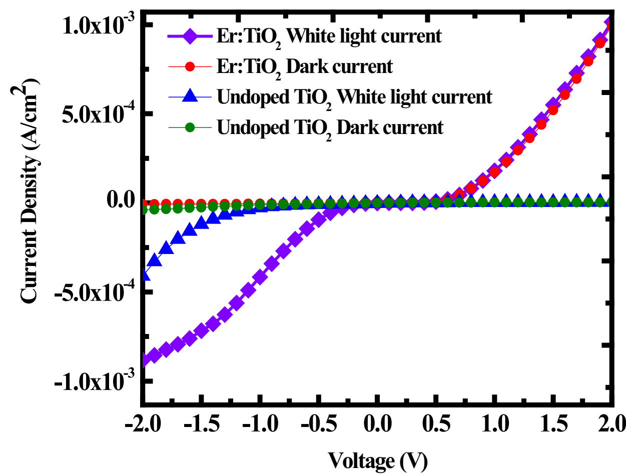

Fig. 5 I–V characteristics of undoped TiO_2 and $Er:TiO_2$ TF detectors under dark and white-light illumination condition

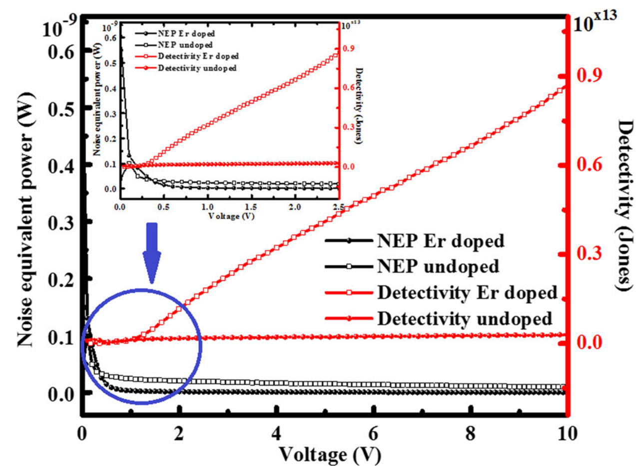

Fig. 6 Noise equivalent power (NEP) and detectivity (D^*) versus the applied voltage at 340 nm for TiO_2 TF detector and $Er:TiO_2$ TF detector

compared to the undoped TiO_2 (2.9×10^{-6} A cm^{-2} at +1.5 V) under dark condition. This high forward current may be due to the increase in defect states (because of the breaking of grain boundaries after Er doping into TiO_2 lattice) at the Au/$Er:TiO_2$ TF interface and corresponding tunneling [41]. Under white light illumination in forward bias for both the undoped and $Er:TiO_2$ TF based detectors, a large number of photo-generated electron–hole pair increases the number of majority carriers and ionizes the interface states [42].

As a result the barrier height increases at the junction and no effective changes in conductivity has been observed of the detectors. Under reverse bias, holes are efficiently trapped by the interface defect states which shrink the depletion region [43] and allow tunneling of electrons. In case of $Er:TiO_2$ detector the presence of large number of traps at the Au/$Er:TiO_2$ TF interface produces efficient trapping of holes and hence tunneling of electrons, and therefore, the high conduction as compared to undoped TiO_2 TF detector [42]. The reverse current of -4.2×10^{-4} A cm^{-2} at −1 V and -2.7×10^{-5} A cm^{-2} at −1 V were recorded for $Er:TiO_2$ TF and undoped TiO_2 TF based detectors, respectively.

Figure 6 shows the detectivity (D^*) and noise equivalent power (NEP) vs applied voltage for both the undoped as well as the $Er:TiO_2$ TF detectors at 340 nm. The NEP and D^* [44] are the figure of merits which are used to analyze the noise performance of the photodetectors. The detectivity is expressed as:

$$D^* = \frac{R_\lambda}{\sqrt{2qJ_{\text{dark}}}} \tag{2}$$

where J_{dark} is the dark current density and R_λ is the responsivity at a particular wavelength and is given as

$$R = \frac{I_{\text{photo}}}{P_{\text{opto}}} \tag{3}$$

where, I_{photo} is the photocurrent and P_{opto} is the optical power. The R_λ at 340 nm monochromatic light illumination at −0.5 V were obtained as 226 and 1.9 mA W^{-1} for $Er:TiO_2$ and undoped TiO_2, respectively.

The NEP is expressed as:

$$\text{NEP} = \frac{\sqrt{A}\sqrt{B}}{D^*} \tag{4}$$

where, A is the detector area and B is the bandwidth which is assumed as 1 kHz in this case as flicker noise is the dominant noise for frequency below 1 kHz for photodetectors [45]. The presence of oxygen defects and dangling bonds gives rise to mobility fluctuations which is responsible for the flicker noise in photodetectors [46].

Figure 6 shows that at 340 nm wavelength the detectivity of the $Er:TiO_2$ is ~5 times more as compared to the undoped TiO_2 at 10 V applied bias and the NEP is also increased from 9.8×10^{-11} W for the undoped TiO_2 to 3.9×10^{-9} W for $Er:TiO_2$ TF detector which illustrates the overall increase in the performance of the $Er:TiO_2$ TF due to the incorporation of Er.

The photo-switching characteristics of undoped and $Er:TiO_2$ at 340 nm at −0.5 V applied bias is shown in Fig. 7. Rise time (T_r) and fall time (T_f) were obtained for both the undoped TiO_2 and $Er:TiO_2$ detector. The T_r is defined as the time required by the pulse to increase from 10 to 90% of its peak value and the T_f is defined as the time required by the pulse to decrease from 90% of the peak value to 10% [44]. At a wavelength of 340 nm, the undoped TiO_2 failed to show any switching characteristic, however, the $Er:TiO_2$ showed a better switching behavior with a T_r of 1.29 s and a T_f of 2.11 s. The current rising

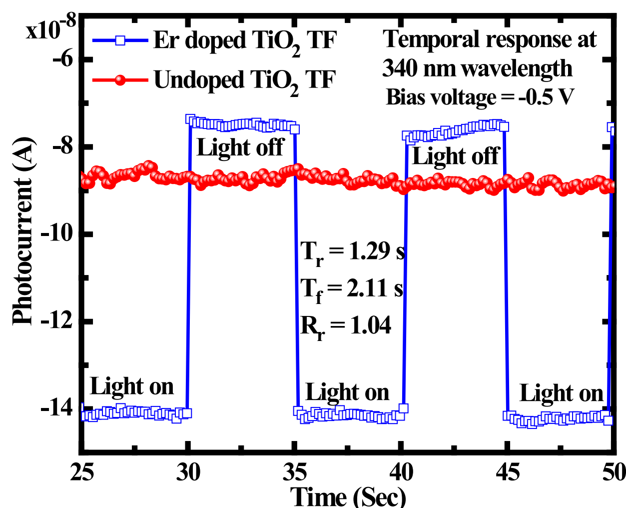

Fig. 7 Photoswitching characteristics of undoped and Er:TiO_2 detectors at 340 nm

ratio (R_r) is defined as the ratio between the maximum and minimum current value of the detector in light on condition. The current value slowly rises from a minimum value to maximum, due to the diffusion of carriers under light on condition for longer time. The drift velocity of the carriers is larger than that of diffusion velocity of the carrier. As a result, the diffused carriers move slowly compared to drift carriers and affects the temporal response of the detector. The R_r is 1.04 for Er:TiO_2 TF detector. The response time of our detector is faster as compared to the TiO_2 NW photodetector reported by Chinnamuthu et al. [47].

From the above experiment it can be concluded that the incident optical power, which enable to produce the photocurrent by generating additional carriers into the Er:TiO_2 TF detector is unable to activate the undoped TiO_2 detector. So, the Er doped detector possesses photo-switching characteristics at particular wavelength (340 nm) and applied voltage of −0.5 V. The fact verifies the high detectivity of the Er:TiO_2 detector at the same wavelength at 340 nm.

4 Conclusion

In summary, the physical vapor deposition technique has been employed to fabricate undoped TiO_2 TF and Er:TiO_2 TF on n-type Si substrate. The FESEM showed well-defined grain boundaries for pure TiO_2 TF which were broken in case of Er:TiO_2 TF due to incorporation of Er in TiO_2. The Raman scattering depicted new Raman bands in case of Er:TiO_2 due to structural deformation of TiO_2 and presence of Er_2O_3 into the structure. The Er:TiO_2 showed an enhancement in the main band gap to 3.2 eV from 3.0 eV (undoped TiO_2) due to the increase in the conduction band level and decrease in the valence band energy levels as a result of substitutional doping of the Er in place of Ti in TiO_2 lattice. From the opto-electronic measurements it was observed that Er:TiO_2 showed an enhancement in the detectivity ∼5 times more as compared to the TiO_2 at 340 nm wavelength. The better temporal response with $T_r = 1.29$ s, $T_f = 2.11$ s was observed for the Er:TiO_2 T-based detector as compared to TiO_2 TF detector. Finally, enhanced photosensitivity was recorded for the Er:TiO_2 TF detectors into UV region.

Acknowledgements The authors would like to acknowledge the COE in Advanced materials of NIT Durgapur for providing the FESEM facility, Dept. of Physics of NIT Nagaland for XRD analysis of the samples and the CRNS, University of Calcutta, for EDAX analysis of the samples. The authors are also grateful to Dr. Ardhendu Saha of NIT Agartala, Department of Electrical Engineering, for providing the optical absorption measurement facility.

References

1. P. Cheong, K. Chang, Y. Lai, S. Ho, I. Sou, K. Tam, IEEE Trans. Ind. Electron. **58**(11), 5271–5277 (2011)
2. S.I. Inamdar, K.Y. Rajpure, J. Alloys Compd. **595**, 55–59 (2014)
3. J.T. Clarke, W.R. Skinner, M.B. Vincent, T. Irgang, V. Suratkal, H. Grassl, J.T. Trauger, Appl. Opt. **38**, 1803–1813 (1999)
4. L. Shi, S. Nihtianov, IEEE Sens. J. **12**, 2453–2459 (2012)
5. G. Bertuccio, D. Puglisi, L. Torrisi, C. Lanzieri, Appl. Surf. Sci. **272**, 128–131 (2013)
6. A. Sciuto, M. Mazzillo, P. Badala, M. Scuderi, B. Carbone, S. Coffa, IEEE Photonics Technol. Lett. **26**, 1782–1785 (2014)
7. X. Sun, D. Li, H. Jiang, Z. Li, H. Song, Y. Chen, G. Miao, Appl. Phys. Lett. **98**, 121117-1–121117-3 (2011)
8. A. Szyszka, L. Lupina, G. Lupina, M. Mazur, M.A. Schubert, P. Storck, S.B. Thapa, T. Schroeder, Appl. Phys. Lett. **104**, 011106-1–011106-5 (2014)
9. F. Xie, H. Lu, D. Chen, X. Ji, F. Yan, R. Zhang, Y. Zheng, L. Li, J. Zhou, IEEE Sens. J. **12**, 2086–2090 (2012)
10. Y.K. Su, S.M. Peng, L.W. Ji, C.Z. Wu, W.B. Cheng, C.H. Liu, Langmuir **26**, 603–606 (2010)
11. G. Cheng, X. Wu, B. Liu, B. Li, X. Zhang, Z. Du, Appl. Phys. Lett. **99**, 203105-1–203105-3 (2011)
12. A.K. Tiwari, A. Mondal, B.K. Mahajan, B. Choudhuri, T. Goswami, M.B. Sarkar, S. Chakrabartty, C. Ngangbam, S. Saha, J. Nanosci. Nanotechnol. **15**, 5099–5104 (2015)
13. A. Mondal, B. Shougaijam, T. Goswami, J.C. Dhar, N.K. Singh, S. Choudhury, K.K. Chattopadhay, Appl. Phys. A **115**, 353–358 (2014)
14. B. Lin, Z. Fu, Y. Jia, Appl. Phys. Lett. **79**, 943–945 (2001)
15. D. Reyes-Coronado, G. Rodríguez-Gattorno, M.E. Espinosa-Pesqueira, C. Cab, R. de Coss, G. Oskam, Nanotechnology **19**, 145605-1–145605-10 (2008)
16. F. Giordano, A. Abate, J. Baena, M. Saliba, T. Matsui, S.H. Im, S.M. Zakeeruddin, M.K. Nazeeruddin, A. Hagfeldt, M. Graetzelb, Nat. Commun. **7**, 10379-1–10379-6 (2016). doi:10.1038/ncomms10379
17. K. Mun, S.D. Alvarez, W. Choi, M.J. Sailor, ACS Nano **4** (4), 2070–2076 (2010)
18. J. Park, T. Jin, C. Liu, G. Li, M. Yan, ACS Omega **1**, 351–356 (2016)
19. Z. Hou, Y. Zhang, K. Deng, Y. Chen, X. Li, X. Deng, Z. Cheng, H. Lian, C. Li, J. Lin, ACS Nano **9**, 2584–2599 (2015)

20. V.G. Deepagan, D.G. You, W. Um, H. Ko, S. Kwon, K.Y. Choi, G. Yi, J.Y. Lee, D.S. Lee, K. Kim, I.C. Kwon, J.H. Park, Nano Lett. **16**, 6257–6264 (2016)
21. P. Chinnamuthu, J.C. Dhar, A. Mondal, A. Bhattacharyya, N.K. Singh, J. Phys. D Appl. Phys. **45**, 135102-1–135102-5 (2012)
22. H. Zhang, S. Ruan, H. Li, M. Zhang, K. Lv, C. Feng, W. Chen, IEEE Electron Device Lett. **33**, 83–85 (2012)
23. B.J. Morgan, G.W. Watson, J. Phys. Chem. C **114**, 2321–2328 (2010)
24. S.R. Johannsen, L.R. Lauridsen, B. Julsgaard, P.T. Neuvonen, S.K. Ram, A.N. Larsen, Thin Solid Films **550**, 499–503 (2014)
25. S.P. Madsen, S.R. Johannsen, B.R. Jeppesen, J.V. Nygaard, P.B. Jensen, J. Chevallier, B. Julsgaard, P. Balling, A.N. Larsen, Energy Procedia **77**, 478–486 (2015)
26. G. Krauss, S. Lohss, T. Hanke, A. Sell, S. Eggert, R. Huber, A. Leitenstorfer, Nat. Photonics **4**, 33–36 (2010)
27. D. Hou, B. Ning, J. Wu, Z. Wang, J. Zhao, Appl. Phys. Lett. **102**, 151104-1–151104-4 (2013)
28. A. Anopchenko, A. Tengattini, A. Marconi, N. Prtljaga, J.M. Ramírez, O. Jambois, Y. Berencén, D. Navarro-Urrios, B. Garrido, F. Milesi, J.-P. Colonna, J.-M. Fedeli, L. Pavesi, J. Appl. Phys. **111**, 063102-1–063102-5 (2012)
29. Anupam Ghosh, Aniruddha Mondal, Avishek Das, Sanatan Chattopadhyay, Kalyan Kumar Chattopadhyay, J. Alloy. Compd. **695**, 1260–1265 (2017)
30. M.B. Sarkar, A. Mondal, B. Choudhuri, B.K. Mahajan, S. Chakrabartty, C. Ngangbam, J. Alloy. Compd. **615**, 440–445 (2014)
31. E.T. Bender, R. Wang, M.T. Aljarrah, E.A. Evans, R.D. Ramsier, J. Vac. Sci. Technol. A **25**, 922–926 (2007)
32. R.J. Deokate, S.M. Pawar, A.V. Moholkar, V.S. Sawant, C.A. Pawar, C.H. Bhosale, K.Y. Rajpure, Appl. Surf. Sci. **254**, 2187–2195 (2008)
33. D.Y. Lee, J. Kim, J. Park, Y. Kim, I. Lee, M. Lee, B. Kim, Curr. Appl. Phys. **13**, 1301–1305 (2013)
34. X. Yu, B. Kim, Y.K. Kim, ACS Catal. **3**, 2479–2486 (2013)
35. Y. Badr, I.K. Battisha, A. Salah, M.A. Salem, Indian J. Pure Appl. Phys. **46**, 706–711 (2008)
36. M.V. Abrashev, N.D. Todorov, J. Geshev, J. Appl. Phys. **116**, 103508-1–103508-7 (2014)
37. R. Palomino-Merino, P. Trejo-Garcia, O. Portillo-Moreno, S. Jiménez-Sandoval, S.A. Tomás, S.A.O. Zelaya-Angel, R. Lozada-Morales, V.M. Castaño, Opt. Mater. **46**, 345–349 (2015)
38. H. Tang, F. Levy, H. Berger, P.E. Schmid, Phys. Rev. B **52**, 7771–7774 (1995)
39. N.R. Mathews, E.R. Morales, M.A. Cortés-Jacome, J.A. Toledo, Antonio. Sol. Energy **83**, 1499–1508 (2009)
40. S. Majumder, D. Paramanik, V. Solanki, B.P. Bag, S. Varma, Appl. Phys. Lett. **98**, 053105-1–053105-3 (2011)
41. D. Scoca, M. Morales, R. Merlo, F. Alvarez, A.R. Zanatta, J. Appl. Phys. **117**, 205304-1–205304-2 (2015)
42. A. Mondal, N.K. Singh, P. Chinnamuthu, J.C. Dhar, A. Bhattacharyya, S. Choudhury, IEEE Photonics Technol. Lett. **24**, 2020–2023 (2012)
43. S.N. Das, K.J. Moon, J.P. Kar, J.H. Choi, J. Xiong, Appl. Phys. Lett. **97**, 022103-1–022103-3 (2010)
44. H. Liu, W. Lin, W. Sun, S. Wei, S. Yu, J. Mater. Sci. Semiconductor Process **57**, 90–94 (2017)
45. S.S. Li, *Semiconductor Physical Electronics*, 2nd edn. (Springer-Verlag, New York, 2006)
46. S. Chang, B. Duan, C. Hsiao, S. Young, B. Wang, T. Kao, K. Tsai, S. Wu, IEEE Photonics Technol. Lett. **25**, 2043–2046 (2013)
47. P. Chinnamuthu, A. Mondal, J.C. Dhar, N.K. Singh, Jpn. J. Appl. Phys. **54**, 06FJ01-1–06FJ01-3 (2015)